Hybrid Overmodulation Strategy of Dual Two-Level Inverter Topology Enabling 12-Step Operation

Filip Baum and Ondrej Lipcak

***Abstract*—This article introduces a novel overmodulation strategy tailored for dual-inverter topologies with galvanically isolated dc-links and evenly distributed dc-link voltage. The core contribution of this article is the utilization of the multilevel capabilities of the dual-inverter topology. At the maximum modulation index, the presented overmodulation method achieves what is referred to as a 12-step operation. The 12-step operation improves the voltage waveform and offers superior harmonic performance compared to the conventional 6-step operation. The utilized approach leverages a hybrid space vector pulsewidth modulation (SVPWM) method, a well-established technique in two-level inverters, to achieve this extended operation range. Furthermore, this article presents a nonlinear gain compensation characteristic vital for real-time motor control applications and provides a comparative analysis of the modulation's harmonic performance. The proposed approach is validated through simulations and experiments. The experiments were conducted using a custom inverter based on Gallium-Nitride transistors where simple volt/hertz control of an induction motor was programmed. The results of these experiments affirm the strategy's effectiveness, showcasing superior current waveform quality and a smooth transition from linear mode to 12-step operation while keeping a simple implementation of the algorithm.**

***Index Terms*—12-step operation, dual-inverter topology, hybrid modulation, motor control, multilevel Inverters, overmodulation.**

I. Introduction

MULTILEVEL voltage source inverters have gained popularity in various industries, including motor control applications, due to their ability to lower total harmonic distortion (THD), improve waveform quality, and reduce voltage stress on semiconductor switching components. These advantages have led to their adoption in a wide range of applications [1], [2], [3]. However, some widely-used multilevel topologies, such as the flying capacitor (FC) and diode-clamped (DC) inverters, face inherent challenges, including the need for capacitor pre-charging [4], [5] and issues related to unbalanced neutral points [6], [7]. In response, numerous modulation strategies have been proposed in the literature, but many of them are highly complex [8].

Manuscript received 11 September 2023; revised 16 November 2023 and 22 December 2023; accepted 21 January 2024. Date of publication 25 January 2024; date of current version 20 March 2024. This work was supported by the Student Grant Competition of the Czech Technical University in Prague under Grant SGS23/111/OHK3/2T/13. Recommended for publication by Associate Editor J. He. *(Corresponding author: Filip Baum.)*

The authors are with the Department of Electric Drives and Traction, Faculty of Electrical Engineering, Czech Technical University in Prague, 166 27 Prague, Czech Republic (e-mail: baumfili@fel.cvut.cz; lipcaond@fel.cvut.cz).

Color versions of one or more figures in this article are available at https://doi.org/10.1109/TPEL.2024.3358407.

Digital Object Identifier 10.1109/TPEL.2024.3358407

In their research, Stemmler and Guggenbach [9] demonstrated that multilevel conversion can be achieved by connecting a conventional two-level voltage-source inverter at each end of an open-winding induction machine (IM). This dual-inverter topology offers distinct advantages, including immunity to neutral-point fluctuations, elimination of capacitor pre-charging, improved fault tolerance, and straightforward control schemes. As a result, it has garnered attention from researchers [10], [11], [12], [13], [14], [15].

The dual-inverter's configuration is categorized into three distinct topologies based on the dc link supply: isolated dc source type, floating capacitor type, and common dc source type. The common dc source configuration is the most compact and cost-effective, with both inverters connected in parallel to a shared dc source. However, this parallel connection can create a path for zero-sequence current (ZSC), potentially affecting drive performance if not addressed in the control algorithm. Consequently, various strategies to eliminate ZSC have been proposed in the literature [15], [16], [17], [18].

In the floating capacitor configuration, one inverter, often called the main inverter, draws power from a standard dc source, while the other, typically referred to as the auxiliary inverter, is connected to a capacitor. This configuration eliminates the ZSC path, allowing for a broader range of control strategies. However, controlling the floating capacitor voltage during runtime adds complexity to the control algorithm. Moreover, fault tolerance is limited compared to other topologies since only faults at the auxiliary inverter side can be resolved [19], [20].

The isolated dc supply topology equips each inverter with its dedicated dc source, eliminating the need for charging and balancing the floating capacitor voltage. This configuration simplifies the control algorithm but increases hardware size, complexity, and cost. While isolating the dc links eliminates the ZSC path, zero-sequence voltage between the two inverters may still occur, potentially leading to shaft or bearing currents [21], [22].

Thanks to the flexibility of the isolated dc supply topology, numerous modulation strategies have been studied and developed in the literature. These strategies are often distinguished by their assumed dc bus voltage ratio, whether equal or unequal. Most strategies assume a 1:1 dc link voltage ratio, leading to behavior similar to a three-level inverter. The dual-inverter topology can be modulated either as two individual two-level inverters, which are modulated separately and combined to generate the desired load voltage [23], [24], [25] or similarly to a conventional

TABLE I
COMPARISON BETWEEN DUAL-INVERTER AND CONVENTIONAL MULTILEVEL INVERTER TOPOLOGIES

	Dual-Inverter	DC-MLI	FC-MLI
Number of DC sources	2 (Isolated)	1	1
Number of volt. levels	3	Any	Any
Number of switches	12	$6(n-1)$	$6(n-1)$
Number of DC-link capacitors	2*	$(n-1)$*	$(n-1)$*
Additional components	No	Diodes	Capacitors
Capacitor balancing	No	Yes	Yes
Overmodulation capability	Yes	Yes	Limited
Square-wave mode capability	Yes	Yes	No
Need to access both winding ends	Yes	No	No

*Multiple capacitors in series or parallel count as one.

three-level inverter, leading to near-state pulsewidth modulation (PWM) [10].

Given that this article utilizes the isolated dc supply configuration with dual two-level inverters, it invites a qualitative comparison with two well-established multilevel inverters—the FC and DC inverters, as shown in Table I. Note that n denotes the number of voltage levels.

One significant advantage of the dual-inverter topology over a single two-level inverter is its superior utilization of dc bus voltage [23], [24], which can be further enhanced through overmodulation. While overmodulation in two-level inverters has been extensively studied [26], [27], its application to the dual-inverter topology has received limited attention.

The most prevalent overmodulation technique for two-level inverters is Bolognani&Zigliotto's hybrid space vector PWM (SVPWM) method, as first published in [28]. This strategy extends the reference voltage vector's circular trajectory beyond the voltage hexagon's boundaries. When the trajectory is within the hexagon boundaries, the modulator operates in a linear mode. When the reference voltage vector goes beyond the hexagon boundaries, the voltage vector corresponding to the intersection of the trajectory and the hexagon is maintained at the output terminals until the reference voltage vector angle becomes smaller than the corresponding sector's center. The switching pattern is then mirrored, enabling a 6-step operation when the reference voltage vector equals the hexagon's circumscribed circle.

This strategy can be extended to the dual-inverter topology, but in its original form, it only achieves 6-step voltage waveforms at the maximum modulation index. However, the dual-inverter topology with equal dc-link voltages allows for an additional 6 fundamental voltage vectors at the hexagon's centers, enabling 12-step operation. The additional vectors increase the number of voltage levels in the output voltage, considerably improving harmonic performance at the cost of a slightly lower voltage gain of the fundamental.

In summary, the contributions of this article can be listed as follows.

1) Extension of Bolognani&Zigliotto's work [28] to a dual-inverter topology with equal in magnitude but galvanically separated inverter dc links.
2) An overmodulation strategy that smoothly transitions from linear to a 12-step operation that offers superior harmonic performance compared to the conventional 6-step operation.
3) In a linear modulation mode, the output voltage vector is synthesized using an SVPWM approach through the reference signal deformation, simplifying implementation significantly.
4) A nonlinear gain function is presented based on Fourier analysis to compensate for voltage gain differences between the reference and actual fundamental voltage components.
5) The conventional Bolognani's overmodulation enabling to reach 6-step operation, and the proposed overmodulation capable of reaching 12-step operation are theoretically compared in terms of their harmonic components.
6) The validation of the proposed modulation strategy is carried out using simulations and experiments. Both employ a simple V/Hz control of IM. Special attention is given to the smooth transition between the overmodulation and the 12-step operation. In addition, the experiments include waveform analysis and THD comparison of the 6-step and 12-step operations.

However, several issues associated with the proposed method should be acknowledged. First, both inverters must operate with the same dc-link voltage, as any significant alteration would shift the fundamental voltage vectors located in the middle of each sector, impeding the proposed method's operation. This issue could be addressed by adopting a generalized overmodulation technique based on the dc-link voltage distribution. Unfortunately, no such technique has been proposed in the literature yet. Second, as this article focuses solely on the overmodulation region, room for additional optimization concerning switching losses exists while operating in the linear region. However, the method's versatility allows for smooth integration with various modulation strategies aimed at reducing switching losses and THD, such as those proposed in [10], [23], and [24]. Finally, the 12-step operation results in a slightly reduced content of the fundamental component compared to the 6-step operation. When increasing the number of voltage levels in the "square wave" mode, a tradeoff always exists between waveform quality and the maximum attainable fundamental voltage component. Nonetheless, the authors firmly believe that the voltage and current waveform quality improvements more than compensate for this reduction.

The rest of this article is organized as follows. Section II provides an overview of the dual-inverter topology focusing on modulation. Section III introduces the proposed modulation strategy, derives the voltage gain characteristic in the overmodulation region, and analyzes low-order harmonic

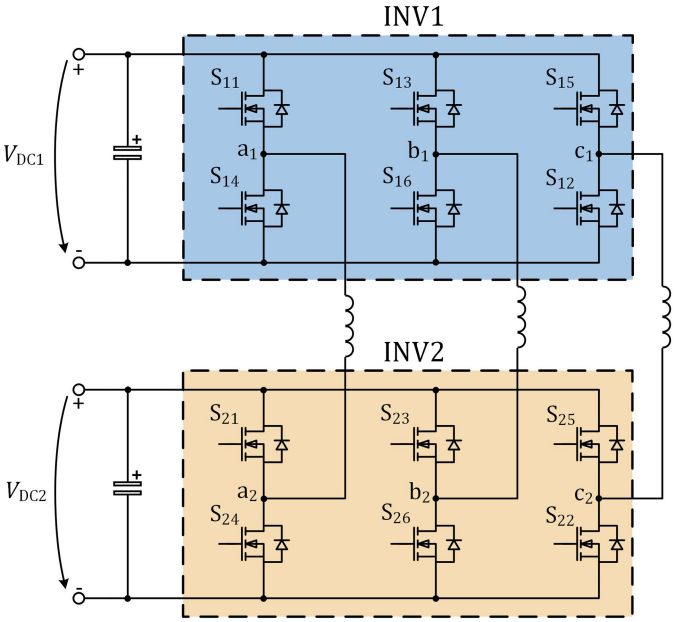

Fig. 1. Dual-inverter open winding topology with isolated DC-links.

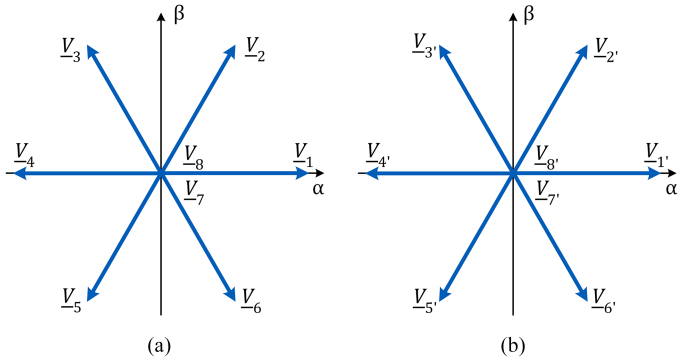

Fig. 2. Fundamental voltage vectors of each inverter. (a) INV1. (b) INV2.

behavior. Finally, Sections IV and V present simulation and experimental results, respectively, to validate the effectiveness of the proposed strategy.

II. Utilized Topology

The dual-inverter open winding topology, as illustrated in Fig. 1, is fed by two isolated dc sources. This approach, which utilizes two separate power supplies and isolates the two dc links, effectively eliminates the ZSC path in the common dc link configuration. The absence of ZSC provides significant modulation flexibility, allowing for the free utilization of all possible switching combinations. This flexibility becomes crucial when the modulation strategy aims to reach the overmodulation region, potentially extending to the square-wave mode of operation.

In this article, we assume equal dc link voltages, i.e., $V_{\mathrm{DC1}} = V_{\mathrm{DC2}}$, and introduce a combined dc link voltage notation:

$$V_{\mathrm{DC}} = V_{\mathrm{DC1}} + V_{\mathrm{DC2}}. \tag{1}$$

As a result, both inverters generate identical fundamental voltage vectors, as depicted in Fig. 2. In a conventional two-level voltage source inverter, there are a total of eight fundamental voltage vectors, denoted as $1-8$ and $1'-8'$ for INV1 and INV2, respectively.

The voltage vectors of the two inverters can be defined as follows:

$$\begin{cases} \underline{V}_{\mathrm{INV1}} = 2\left(v_{\mathrm{a1o}} + v_{\mathrm{b1o}}\mathrm{e}^{\mathrm{j}2\pi/3} + v_{\mathrm{c1o}}\mathrm{e}^{-\mathrm{j}2\pi/3}\right)/3 \\ \underline{V}_{\mathrm{INV2}} = 2\left(v_{\mathrm{a2o}} + v_{\mathrm{b2o}}\mathrm{e}^{\mathrm{j}2\pi/3} + v_{\mathrm{c2o}}\mathrm{e}^{-\mathrm{j}2\pi/3}\right)/3 \end{cases} \tag{2}$$

where $v_{k1\mathrm{o}}$ and $v_{k2\mathrm{o}}$ are the pole voltages of the two inverters, respectively, $(k = \mathrm{a},\ \mathrm{b},\ \mathrm{c})$. Furthermore, by examining Fig. 1, the motor phase voltages can be expressed as

$$\begin{cases} v_{\mathrm{a}} = v_{\mathrm{a1a2}} = v_{\mathrm{a1o}} - v_{\mathrm{a2o}} \\ v_{\mathrm{b}} = v_{\mathrm{b1b2}} = v_{\mathrm{b1o}} - v_{\mathrm{b2o}} \\ v_{\mathrm{c}} = v_{\mathrm{c1c2}} = v_{\mathrm{c1o}} - v_{\mathrm{c2o}} \end{cases}. \tag{3}$$

Based on (2) and (3), the resulting voltage vector of the dual-inverter topology is obtained by subtracting $\underline{V}_{\mathrm{INV2}}$ from $\underline{V}_{\mathrm{INV1}}$

$$\underline{V} = \underline{V}_{\mathrm{INV1}} - \underline{V}_{\mathrm{INV2}}. \tag{4}$$

Each inverter can operate with eight different switching states, resulting in 64 possible combinations of switching states and 19 unique voltage vectors, including 18 active vectors and 1 zero vector [17]. If the dc-link voltages become unequal, some switching combinations connect the dc-link capacitors in parallel. Consequently, undesirable in-rush current spikes occur as the capacitor with higher voltage chargers the other. Therefore, these switching combinations should be avoided [11]. The complete set of voltage vectors of the dual-inverter, along with the corresponding states of each inverter, is depicted in Fig. 3. For instance, $15'$ signifies that vectors $\underline{V}_1$ and $\underline{V}_{5'}$ are generated by INV1 and INV2, respectively, to produce the resulting voltage vector.

Given the isolated dc links, one modulation approach for the dual-inverter is to treat it as two individual two-level inverters working together to generate the desired voltage. This approach allows the utilization of well-established modulation techniques, such as SVPWM or various bus-clamping strategies [23], [24], for each of the two inverters. In this article, we employ conventional SVPWM for both inverters.

Combining the outputs of the two inverters to generate the desired voltage vector is accomplished using (4). First, the reference voltage vector $\underline{v}^*$ coming from the motor control algorithm is split into two sub-vectors $\underline{v}^*_{\mathrm{INV1}}$ and $\underline{v}^*_{\mathrm{INV2}}$. Assuming $V_{\mathrm{DC1}} = V_{\mathrm{DC1}}$, the subvectors have equal magnitudes, i.e.,

$$|\underline{v}^*_{\mathrm{INV1}}| = |\underline{v}^*_{\mathrm{INV2}}| = \frac{|\underline{v}^*|}{2}. \tag{5}$$

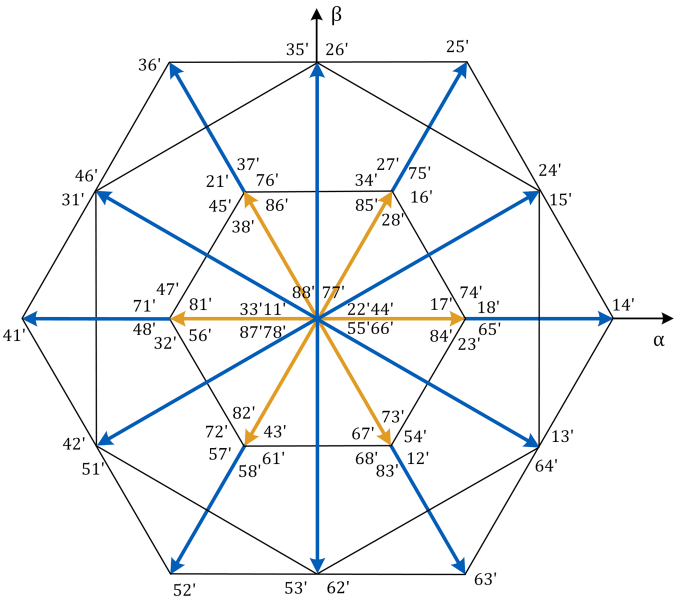

Fig. 3. Fundamental voltage vectors of the dual-inverter topology.

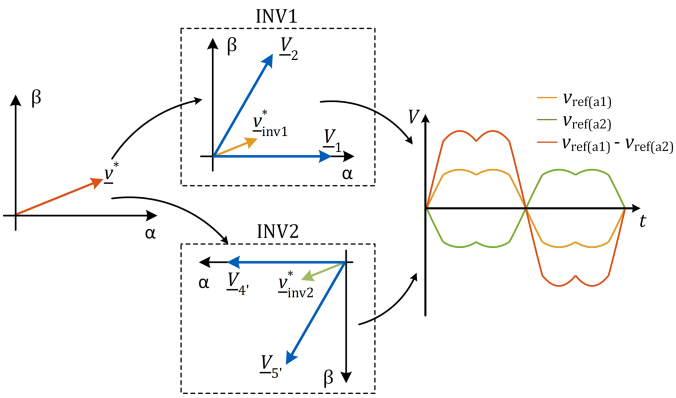

Fig. 4. Reference voltage vector distribution between the two inverters in the dual-inverter topology.

Regarding the phase, it holds that

$$\begin{cases} \arg\left(\underline{v}_{\text{INV1}}\right) = \arg\left(\underline{v}^*\right) \\ \arg\left(\underline{v}_{\text{INV2}}\right) = \arg\left(\underline{v}_{\text{INV1}}\right) + \pi \end{cases}. \tag{6}$$

To satisfy (4), the reference sub-vector for INV2 is phase-shifted by 180°. Consequently, during every modulation period, both inverters synthesize a voltage vector of equal magnitude but of opposite phase, as illustrated in Fig. 4. Furthermore, for completeness, the figure also includes the resulting reference voltages for the phase "a."

One of the most prevalent overmodulation techniques for a two-level inverter in the literature is Bolognani's method, first published in [28]. This method offers straightforward implementation, nearly linear gain characteristics, and minimal phase distortion. This method can be used for the dual-inverter topology without modifications. If the reference voltage vector-splitting

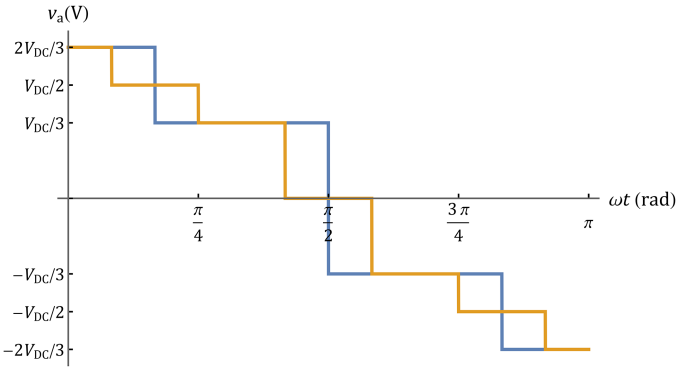

Fig. 5. Phase "a" voltage—comparison of 6-step (blue) and 12-step (orange) operation.

method is employed, both inverters would enter the overmodulation region simultaneously and continue to the square-wave mode of operation. In this mode, the output voltage waveform would be identical to that generated by a single two-level inverter, utilizing only the six fundamental active voltage vectors of each inverter from Fig. 2. This operating mode, referred to as the 6-step mode, corresponds to the number of switchovers per fundamental cycle. The fundamental output voltage component magnitude in a 6-step mode can be written as [29]

$$|v_1| = \frac{2}{\pi} V_{\text{DC}} \approx 0.636\, V_{\text{DC}}. \tag{7}$$

The dual-inverter topology, however, has the capability to generate multilevel waveforms. Examining the voltage vectors in Fig. 3 shows that 12 vectors reach the outer hexagon boundary. The vectors located at the vertexes of the hexagon have a magnitude of $2V_{\text{DC}}/3$, while those located between two vertexes have a magnitude of $V_{\text{DC}}/\sqrt{3}$. Applying each of these vectors for 1/12 of the fundamental cycle generates a three-level waveform identical to the one produced by a conventional three-level inverter. This operating mode, denoted as the 12-step mode, is illustrated in Fig. 5. The fundamental voltage component magnitude in the 12-step operation can be expressed as [29]

$$|v_1| = \frac{\sqrt{2+\sqrt{3}}}{\pi} V_{\text{DC}} \approx 0.615\, V_{\text{DC}}. \tag{8}$$

Despite a slight decrease of 3.4% in the magnitude of the fundamental component compared to the 6-step operation, the authors believe that the improvements in waveform quality more than compensate for this reduction. The 12-step operation results in higher voltage quality, leading to lower current distortion and reduced torque ripple and motor and inverter losses, ultimately improving drive performance [1].

III. Proposed Modulation Strategy

Fig. 6 illustrates the working principle of the proposed modulation strategy for the first sector of the global voltage hexagon.

1) The reference voltage vector $\underline{v}^*{}_{\text{mod}}$ is introduced. The subscript "mod" signifies that this is a modified reference

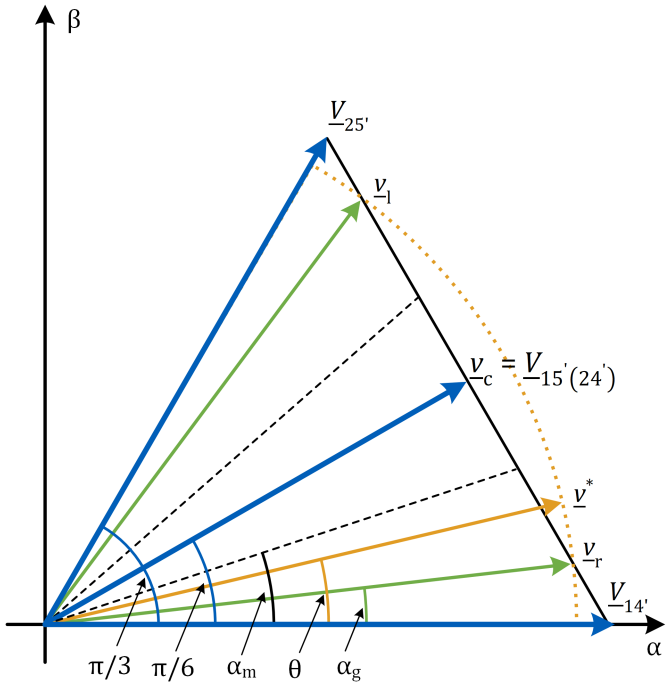

Fig. 6. Principle of the proposed overmodulation strategy—Sector 1.

vector since it must be adjusted in the overmodulation region to achieve the desired fundamental output voltage component. The modified voltage vector is expressed as

$$\underline{v}^*_{\text{mod}} = v^*_{\text{mod}}\, e^{j\theta} \tag{9}$$

$$v^*_{\text{mod}} = \frac{V_{\text{DC}}}{\sqrt{3}\cos\left(\frac{\pi}{6} - \alpha_g\right)}. \tag{10}$$

2) In the interval $0 \le \theta \le \alpha_g$, the modulator operates in the linear region, and no modification is needed.
3) In the interval $\alpha_g \le \theta \le \alpha_m$, the reference voltage vector exceeds the hexagon boundary. The angle α_m is defined as

$$\alpha_m = \frac{\pi}{12} - \frac{\alpha_g}{2}. \tag{11}$$

Here, the output voltage vector $\underline{v}_r$ corresponds to the intersections of $\underline{v}^*_{\text{mod}}$ with the hexagon boundary. This vector needs to be modulated. It can be expressed as

$$\underline{v}_r = v_{\text{ref}}\, e^{j\alpha_g}. \tag{12}$$

4) When $\alpha_m \le \theta \le \pi/6$, the output voltage vector equals to $\underline{v}_c$ which is one of the fundamental voltage vectors (vector 15') of the inverter

$$\underline{v}_c = \frac{U_{\text{DC}}}{\sqrt{3}}\, e^{j\frac{\pi}{6}}. \tag{13}$$

5) No modulation is needed here since the vector corresponds to a specific switching combination.
6) The vector $\underline{v}_c$ is kept at the inverter output also in the interval $\pi/6 \le \theta \le \alpha'_m$. The angle α'_m is defined as

$$\alpha'_m = \frac{\pi}{3} - \alpha_m. \tag{14}$$

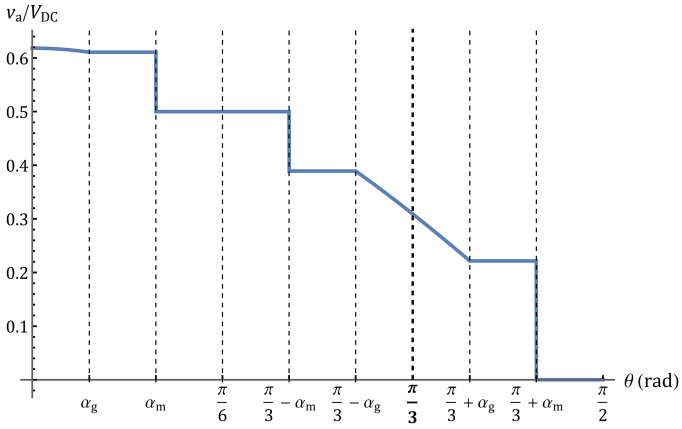

Fig. 7. Output phase "a" voltage waveform of the proposed modulation strategy for an "infinite" switching frequency.

However, symmetry conservation makes the fundamental voltage vector now synthesized as 24' instead of 15'.

7) In the interval $\alpha'_m \le \theta \le \alpha'_g$, where

$$\alpha'_g = \frac{\pi}{3} - \alpha_g. \tag{15}$$

The output voltage vector is $\underline{v}_l$, which is $\underline{v}_r$ mirrored around $\underline{v}_c$

$$\underline{v}_l = v_{\text{ref}}\, e^{j\alpha'_g}. \tag{16}$$

8) Finally, when $\alpha'_g \le \theta \le \pi/3$, the inverter operates again in a linear modulation mode.

The output voltage vector can be expressed as a piecewise function

$$\underline{v}_{\text{out}}(\theta) = \begin{cases} \underline{v}^*_{\text{mod}}, & 0 \le \theta < \alpha_g \\ \underline{v}_r, & \alpha_g \le \theta < \alpha_m \\ \underline{v}_c, & \alpha_m \le \theta < \pi/6 \\ \underline{v}_c, & \pi/6 \le \theta < \alpha'_m \\ \underline{v}_l, & \alpha'_m \le \theta < \alpha'_g \\ \underline{v}^*_{\text{mod}}, & \alpha'_g \le \theta < \pi/6 \end{cases}. \tag{17}$$

In the context of overmodulation strategies, a formula that describes the relationship between the reference and actual voltage is vital. The nonlinear gain function will be derived for the phase "a" voltage, which is the projection of (17) into the real axis. Specifically, for the first sector depicted in Fig. 6, the phase "a" voltage can be written as

$$v_a(\theta) = \begin{cases} v^*_{\text{mod}}\cos\theta, & 0 \le \theta < \alpha_g \\ v^*_{\text{mod}}\cos\alpha_g, & \alpha_g \le \theta < \alpha_m \\ V_{\text{DC}}/2, & \alpha_m \le \theta < \pi/6 \\ V_{\text{DC}}/2, & \pi/6 \le \theta < \alpha'_m \\ v^*_{\text{mod}}\cos\alpha'_g, & \alpha'_m \le \theta < \alpha'_g \\ v^*_{\text{mod}}\cos\theta, & \alpha'_g \le \theta < \pi/6 \end{cases}. \tag{18}$$

The output voltage waveform related to V_{DC} is depicted in Fig. 7. In the figure, the waveform is extrapolated to $\pi/2$ to capture one quarter of the fundamental's period.

The νth odd harmonic of the output voltage, excluding the triplet harmonics, can be calculated through Fourier analysis

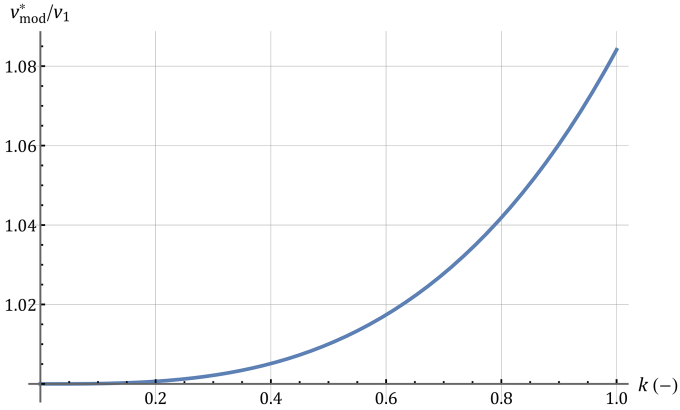

Fig. 8. Ratio of the modified voltage amplitude to the actual fundamental output voltage component as a function of the variable k.

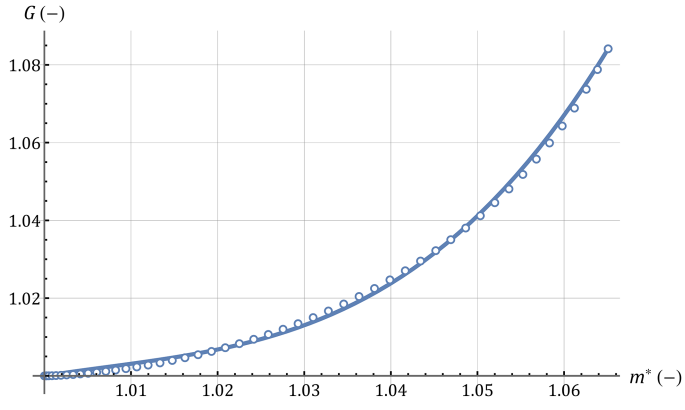

Fig. 9. Nonlinear gain function suitable for compensating the reference voltage vector magnitude in the control algorithm before it enters the modulator.

using the following expression:

$$v_\nu = \frac{4}{\pi} \int_0^{\pi/2} v_\mathrm{a}(\theta) \cos \nu\theta \, \mathrm{d}\theta. \tag{19}$$

It is important to note that (19) also includes even harmonics due to integrating over one-quarter of the output periodic waveform. In addition, it is worth emphasizing that during the instants, when the output voltage is modulated, the switching frequency is expected to be significantly higher, ideally infinite, compared to the frequency of the fundamental. Consequently, we can consider the output voltage to be determined solely by its average value over a modulation period.

Upon performing the integration, the fundamental component can be expressed as

$$v_1 = \frac{V_\mathrm{DC}\left(\pi - k\pi + 3\sin\frac{k\pi}{12} + 3\sin\frac{k\pi}{4}\right)}{\sqrt{3}\pi\cos\frac{k\pi}{6}}. \tag{20}$$

Here, the parameter k is related to the angle α_g by the substitution

$$\alpha_\mathrm{g} = \frac{\pi}{6}(1-k). \tag{21}$$

This substitution normalizes the dependence within the range $\langle 0,\ 1\rangle$, ensuring that an increase in the independent variable corresponds to an increase in the output voltage. Specifically, using the angle α_g, the maximum voltage is achieved when $\alpha_\mathrm{g} = 0$.

Fig. 8 then illustrates the relationship between the ratio of the modified voltage vector v^*_mod, which has been rewritten as a function of the variable k

$$v^*_\mathrm{mod} = \frac{V_\mathrm{DC}}{\sqrt{3}\cos\left(\frac{k\pi}{6}\right)} \tag{22}$$

and the fundamental output voltage component amplitude is given as (20). The ratio defines the voltage gain

$$G = \frac{v^*_\mathrm{mod}}{v_1} = \frac{\pi}{\pi - k\pi + 3\sin\frac{k\pi}{12} + 3\sin\frac{k\pi}{4}}. \tag{23}$$

However, it is worth noting that (23) is not directly usable for adjusting the reference voltage in motor control strategies. Instead, a nonlinear gain function is needed to adjust the reference voltage vector based on a reference modulation index. The modulation index m is defined here as the ratio of the magnitude of the reference voltage vector within the control algorithm, which represents the desired fundamental output voltage component, to the maximum output voltage in a linear mode (when inverter nonidealities are neglected). In mathematical terms

$$m = \frac{v^*}{V_\mathrm{DC}/\sqrt{3}} = \frac{v_1}{V_\mathrm{DC}/\sqrt{3}}. \tag{24}$$

Substituting (20) to (24) yields

$$m = \frac{\pi - k\pi + 3\sin\frac{k\pi}{12} + 3\sin\frac{k\pi}{4}}{\pi\cos\frac{k\pi}{6}}. \tag{25}$$

The objective now is to express (23) as a function of m, i.e., $G = f(m)$. Unfortunately, this task must be handled numerically because it cannot be solved analytically. The steps can be summarized as follows.

1) Evaluate the dependence given by (25) at a finite number of points by iterating over k.
2) Create a table with m on the x-axis and G on the y-axis using (23) and the same set of iterations of k.

The resulting relationship is depicted in Fig. 9. The circles represent the evaluated discrete points (50 points). While the dependence can be readily implemented as a lookup table, it is possible to interpolate the points with sufficient accuracy using a third-order polynomial of the form

$$G = 333.1m^3 - 1006.5m^2 + 1014.03m - 339.643. \tag{26}$$

The interpolated curve using (26) is presented in Fig. 9 as a solid line.

A. Harmonic Behavior

In the context of overmodulation strategies, assessing the harmonic content of the output voltage waveform, especially the low-order harmonics, is of great importance in evaluating the

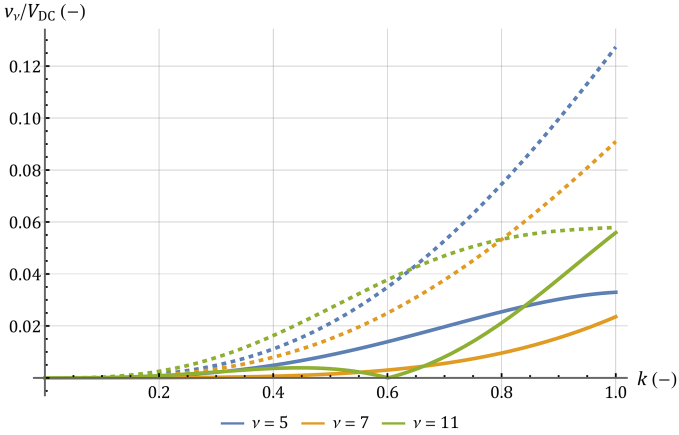

Fig. 10. Low order harmonics—solid: proposed modulation strategy, dashed: Bolognani's modulation.

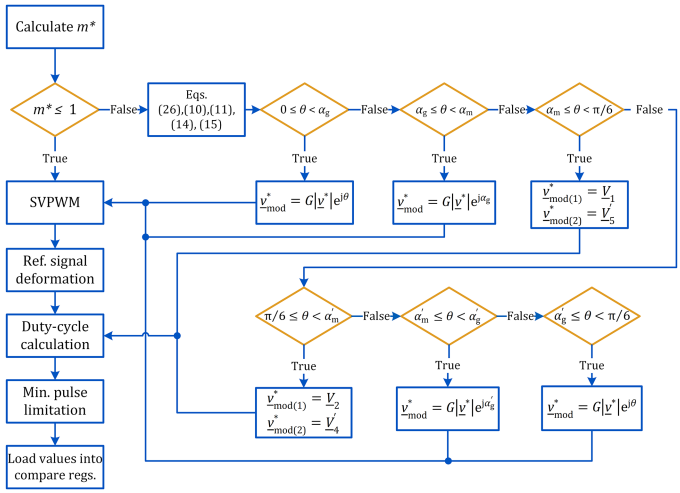

Fig. 11. Flowchart addressing the inner implementation of the modulator.

quality of the motor current waveform. To gain a comprehensive understanding of harmonic behavior, (19) has been further analyzed for the 5th, 7th, and 11th harmonic, resulting in the following expressions:

$$v_5 = -\frac{V_{DC}\left(3\sin\frac{k\pi}{4} - 3\sin\frac{7k\pi}{12} + \sin k\pi\right)}{5\sqrt{3}\pi\cos\frac{k\pi}{6}} \tag{27}$$

$$v_7 = \frac{V_{DC}\left(3\sin\frac{5k\pi}{12} - 3\sin\frac{3k\pi}{4} + \sin k\pi\right)}{7\sqrt{3}\pi\cos\frac{k\pi}{6}} \tag{28}$$

$$v_{11} = \frac{V_{DC}\left(6\sin\frac{3k\pi}{4} - 6\sin\frac{13k\pi}{12} + \sin 2k\pi\right)}{22\sqrt{3}\pi\cos\frac{k\pi}{6}}. \tag{29}$$

These equations provide insights into the amplitudes of the output voltage's 5th, 7th, and 11th harmonic components. Their absolute values are illustrated in Fig. 10 as solid lines. For comparative analysis, the corresponding harmonics resulting from Bolognani's modulation strategy [28] are also depicted in the figure as dashed lines. Notably, the proposed modulation strategy, which enables a 12-step operation of the dual-inverter topology, exhibits superior harmonic behavior compared to the traditional overmodulation strategy that achieves the classical 6-step operation.

B. Implementation of Modulator

The inner workings of the modulator are illustrated in the flowchart presented in Fig. 11.

The modulator operation is contingent on the calculated reference modulation index, denoted as m, as derived from (24). The modulator's behavior can be summarized as follows.

Linear Region ($\boldsymbol{m \leq 1}$)*:* If m is less than or equal to 1, indicating operation within the linear region, the modulator implements the standard SVPWM. This article employs the reference signal deformation approach to SVPWM for its exceptional implementation simplicity. In this approach, the reference voltages generated by the control algorithm are modified by a zero-sequence component defined as

$$v''_x = v^*_x - v_0,\ x = \mathrm{a}, \mathrm{b}, \mathrm{c} \tag{30}$$

where the zero-sequence component v_0 is calculated as [30]

$$v_0 = \frac{\max\left(v^*_\mathrm{a}, v^*_\mathrm{b}, v^*_\mathrm{c}\right) + \min\left(v^*_\mathrm{a}, v^*_\mathrm{b}, v^*_\mathrm{c}\right)}{2}. \tag{31}$$

Subsequently, the modulator computes the values for the PWM compare registers while adhering to the minimum pulse duration constraints. These values are then loaded into their respective registers.

Overmodulation Region ($\boldsymbol{m > 1}$)*:* When m exceeds 1, indicating entry into the overmodulation region, the modulator initiates a different operation. Initially, it calculates the gain using (26), which allows the modulator to adjust the reference voltage vector.

Next, the sector in which the reference vector is positioned is determined using the equation:

$$s = \mathrm{mod}\left(\mathrm{atan2}\left(\frac{v_\beta}{v_\alpha}\right), \frac{\pi}{3}\right) + 1. \tag{32}$$

To simplify the modulator structure, the reference vector is rotated to the first sector

$$\underline{v}^*_{\mathrm{mod(rot)}} = |\underline{v}^*_{\mathrm{mod}}|e^{\mathrm{j}\theta_{\mathrm{rot}}} \tag{33}$$

where θ_{rot} is calculated as

$$\theta_{\mathrm{rot}} = \theta - (s-1)\frac{\pi}{3},\ s = 1\ldots 6. \tag{34}$$

By performing this rotation, the modulator only needs to be implemented for sector 1, with adjustments made based on the actual reference vector position if necessary.

After scaling and rotating the reference vector, the intersection angle α_g is determined using (10). Subsequently, the remaining significant angles, namely α_m, α'_m, and α'_g, are calculated as per (11), (14), and (15), respectively.

Finally, the modulator synthesizes the output voltage vector based on the rotated reference vector position within sector 1 using (17). If $\underline{v}^*_{\mathrm{mod}}$ is situated outside of sector 1, the intersection vectors $\underline{v}_\mathrm{r}$ and $\underline{v}_\mathrm{l}$ must be rotated back to the corresponding sector before modulation. Likewise, the vector $\underline{v}_\mathrm{c}$ is generated

TABLE II
IM NAMEPLATE DATA AND MODEL PARAMETERS—SIMULATION SETUP

Nominal power	12 kW
Nominal frequency	50 Hz
Nominal voltage	400 V
Nominal current	22 A
Nominal speed	1460 min^{-1}
Number of poles	4
Nominal power factor	0.8
Stator resistance	377 mΩ
Rotor resistance	225 mΩ
Stat. leak. inductance	2.27 mH
Rot. leak. inductance	2.27 mH
Mag. inductance	82.5 mH

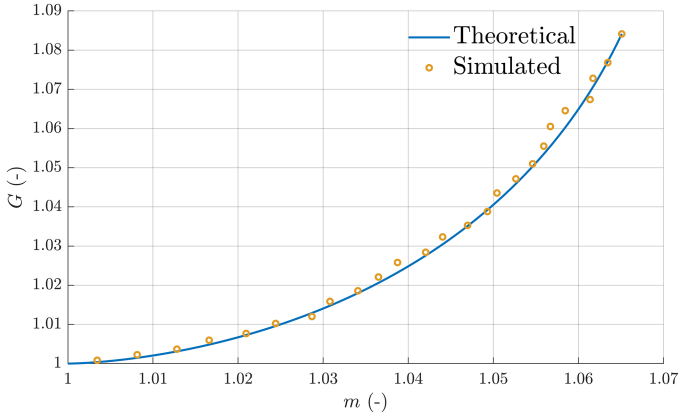

Fig. 12. Verification of the derived gain compensation function.

based on the actual position of $\underline{v}^*_{\text{mod}}$ since each sector requires a different switching combination.

Regarding computational complexity, Bolognani's method, upon which the proposed strategy is built, inherently requires less computational effort. First, only three threshold angles α_{g}, $\pi/6$, and α'_{g}, are checked. Second, the compensation gain function can be approximated by a first-degree polynomial with sufficient accuracy, as demonstrated in [28], resulting in a more straightforward expression compared to (26). The remaining calculations, namely sector determination and reference vector rotation, remain identical.

In addition, it is advisable to constrain the value of the intersection angle α_{g} within the range of $\langle 0, \pi/6 \rangle$ to prevent it from exceeding bounds and potentially compromising the modulation algorithm. Explicitly limiting α_{g} to a specific minimum and maximum values is redundant, as the minimum pulse duration constraint implicitly addresses this concern.

This comprehensive modulator design ensures effective control and modulation of the dual-inverter system, allowing a seamless transition between linear and overmodulation regions while optimizing performance and maintaining harmonic quality.

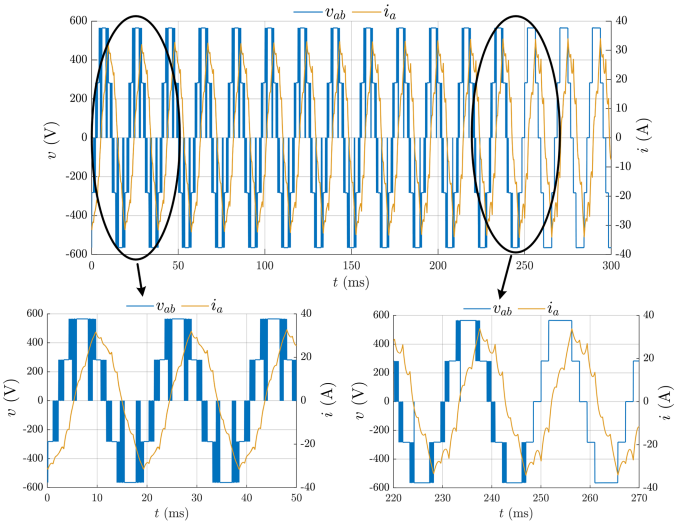

Fig. 13. Detail of motor line-to-line voltage and phase current during the transfer between the linear modulation mode and 12-step operation.

IV. SIMULATION RESULTS

Numerical simulations were conducted in the MATLAB/Simulink environment to validate the proposed overmodulation strategy and further substantiate the experimental findings. To align the simulation setup with the experiments, a simple V/Hz control of an IM was implemented analogously to Fig. 15. Moreover, the simulations were performed using a higher power machine compared to the experiments to validate the proposed method on a system with a different power rating. Refer to Table II for the machine parameters.

The simulation setup included the following configurations.

1) The machine and inverters were modeled using blocks from the Simscape library.
2) The global Simulink solver was set to ode2 with a fixed-step size of 500 ns.
3) The local Simscape solver was set to "trapezoidal" with an identical step size.
4) The switching frequency was set to 20 kHz to ensure an adequate ratio to the simulation step size and to match the switching frequency used in the subsequent experiments.

Fig. 12 illustrates the comparison of the actual simulated gain of the proposed method with the theoretical dependence (26). These results affirm the correctness and accuracy of the theoretical analysis presented in previous sections. The mere differences are attributed mainly to finite sample time and numerics.

The top part of Fig. 13 demonstrates the modulator's progression through the overmodulation region to the 12-step operation. The bottom-left figure illustrates the modulator's operation at approximately halfway between the linear region and the 12-step operation. Meanwhile, the figure in the bottom-right highlights the transition to the 12-step operation. Similarly, Fig. 14 displays the modulator entering the overmodulation region, with the bottom-left figure emphasizing the transition from the linear region to the overmodulation region. In all cases, the transitions are seamless without voltage waveform irregularities and unwanted current overshoots.

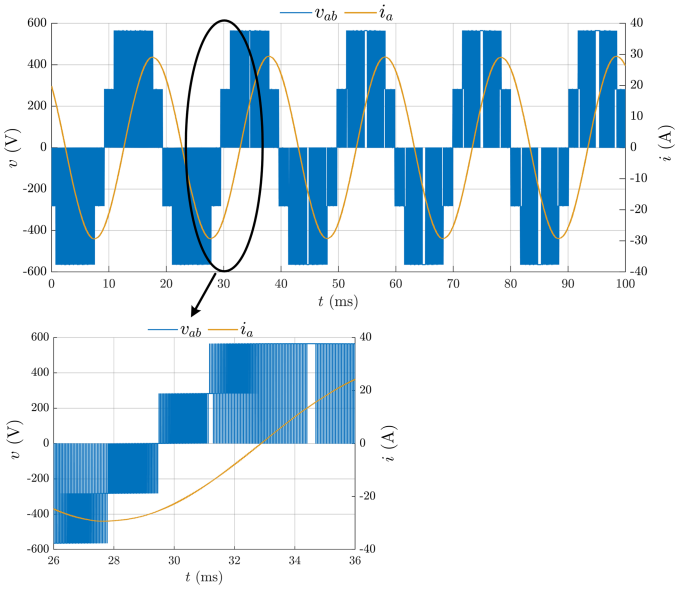

Fig. 14. Detail of motor line-to-line voltage and phase current during the transition from linear region into overmodulation.

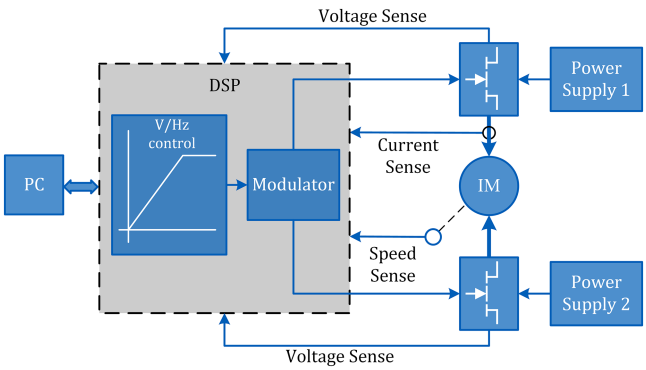

Fig. 15. Block diagram of the experimental setup.

V. Experimental Results

A. Experimental Setup Description

A block diagram of the experimental setup is depicted in Fig. 15. A picture of the experimental setup is then shown in Fig. 16. The inverter is based on Gallium-Nitride (GaN) transistors GS66516T-TR from GaN Systems. The dead time for the transistors has been selected as 100 ns, and the minimum control pulse width as 200 ns. The switching frequency has been set to 20 kHz. Although GaN devices can achieve much higher frequencies, the switching frequency has been intentionally lower due to oscilloscope sampling problems at more expansive waveform windows (hundreds of ms). The inverter is supplied from two galvanically isolated laboratory dc sources—each voltage has been set to 48 V. The motor currents and dc-link voltages are sensed by sigma-delta converters. The motor speed is then measured by a tachodynamo mounted on the motor shaft.

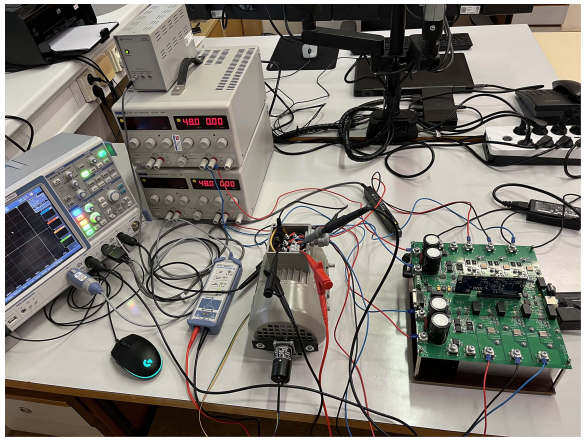

Fig. 16. Picture of the experimental setup.

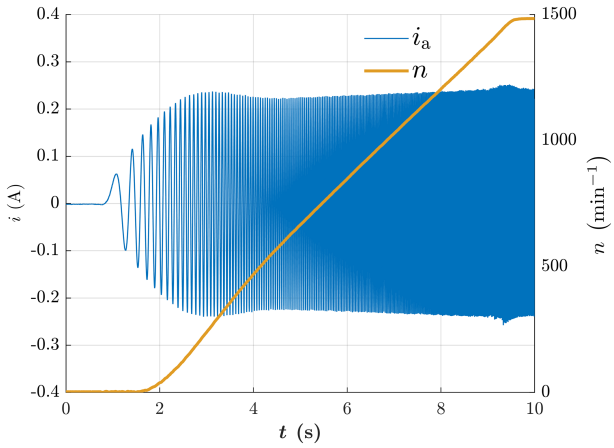

Fig. 17. Acceleration of the motor using the programmed volt-hertz control.

The whole dual-inverter is controlled by a TMDSCNCD28379D processor card from Texas Instruments, which has been programmed in C.

B. Measured Results

For the experimental validation of the proposed modulation strategy, a simple volt/hertz control using a small IM (for IM parameters, refer to Table III) was employed, as illustrated in Fig. 15. The results obtained from these experiments are presented below.

Fig. 17 displays the motor's acceleration under the programmed volt-hertz control. The graph showcases both motor speed and phase "a" current. Notably, the acceleration ramp is configured so that the motor operates in a 12-step mode at the target frequency of 50 Hz.

The detail of the transfer from the linear modulation mode to 12-step operation is depicted in Fig. 18. Here, it is essential to note that the current recorded is the phase "a" current i_a but the voltage is the line-to-line voltage v_{ab}. Since the voltage v_{ab} is given by the difference in voltage v_a and v_b, the noise caused by the rapid switching of GaN transistors superimposed on the voltage probes is eliminated.

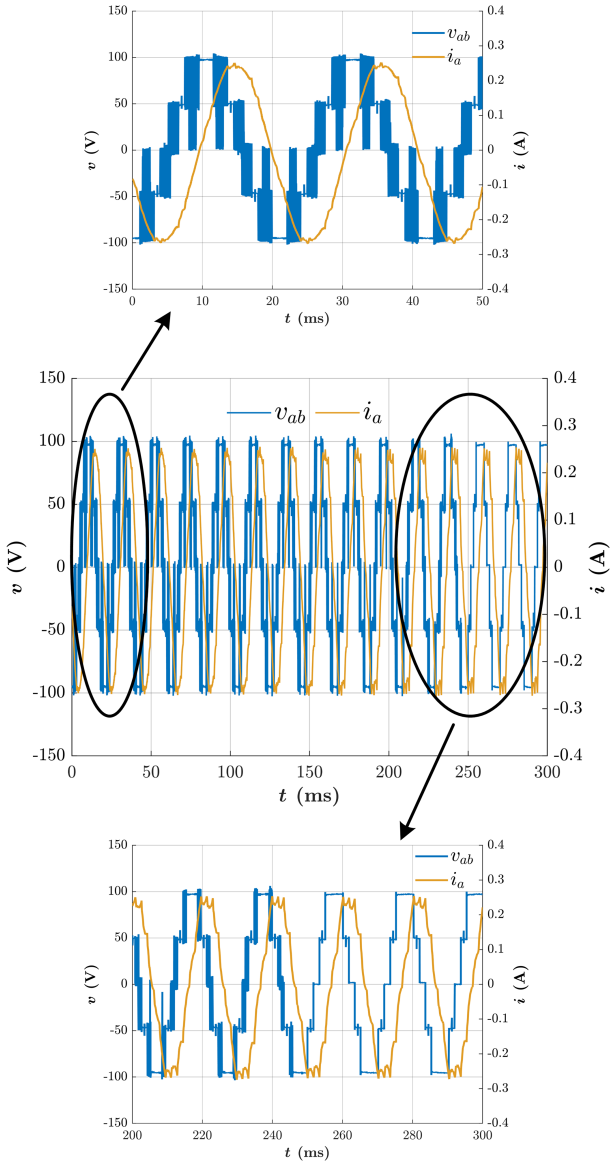

Fig. 18. Detail of motor line-to-line voltage and phase current during the transfer between the linear modulation mode and 12-step operation.

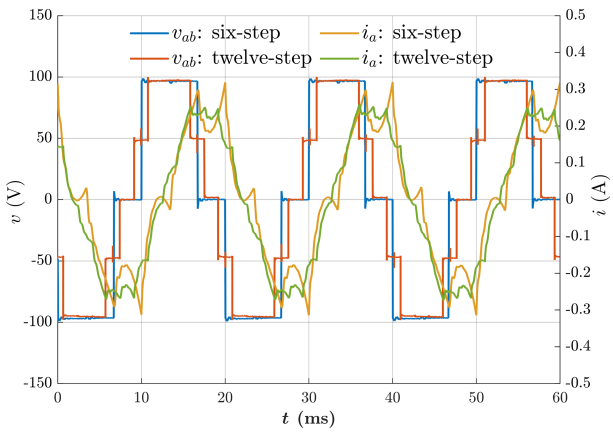

Fig. 19. Comparison of the 12-step and 6-step operations regarding phase current and line-to-line voltage.

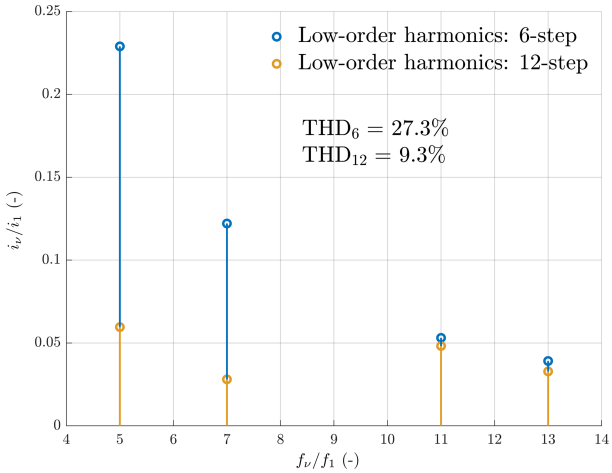

Fig. 20. Quantitative comparison of the harmonic performance of the phase current waveforms from the previous figure.

TABLE III
IM NAMEPLATE DATA AND MODEL PARAMETERS—EXPERIMENTAL SETUP

Nominal power	0.37 kW
Nominal frequency	50 Hz
Nominal voltage	230/400 V (Δ/Y)
Nominal current	1.82/1.05 A
Nominal speed	1460 min^{-1}
Number of poles	4
Nominal power factor	0.78
Stator resistance	27.58 Ω
Rotor resistance	24.97 Ω
Stat. leak. inductance	69.7 mH
Rot. leak. inductance	69.7 mH
Mag. inductance	620.7 mH

The top part of Fig. 18 shows approximately the half-way between the end of the linear mode and the beginning of the 12-step operation. The bottom of Fig. 18 then shows the modulator entering the 12-step operation. Overall, it can be stated that the transition of the proposed modulator into the 12-step operation is smooth both from the perspective of the motor current and voltage.

Fig. 19 offers a direct comparison of a 6-step and 12-step operation again in terms of i_a and v_ab. Even though the voltage gain of the fundamental is slightly lower in the 12-step operation, the voltage, and consequently, the current waveform quality, is superior compared to 6-step operation when the currents are highly distorted by the low-order harmonics.

Finally, Fig. 20 quantitatively compares the harmonic behavior of the current waveforms shown in Fig. 19. The figure shows the ratio of the 5th, 7th, 11th, and 13th harmonic to the fundamental also the overall THD calculated as the RMS amplitude of the harmonics to the RMS amplitude of the fundamental. In the context of electric drives, the superior harmonic performance of the 12-step operation goes hand in hand with the lower inverter and motor copper and iron losses.

VI. Conclusion

In conclusion, a novel hybrid overmodulation strategy was presented in this article for the dual two-level inverter topology with isolated dc-links. The proposed strategy achieved a seamless transition from linear to 12-step operation, resulting in a significant reduction in harmonic distortion of the output current compared to conventional 6-step operation. The proposed strategy is based on hybrid SVPWM, a well-known modulation technique in two-level inverters, which was modified to fully utilize the dual-inverter topology's multilevel capabilities. Standard SVPWM using the reference signal deformation approach was employed in the linear region, leading to substantial algorithm simplification, and reduced computational complexity.

As a result of harmonic analysis, a nonlinear gain function was derived to compensate for voltage gain differences between the reference and actual fundamental voltage components. Furthermore, closed-form expressions for low-order harmonics were presented and compared with those of the original Bolognani's method.

Experimental verification of the proposed method was conducted on a custom-made inverter based on GaN devices, where simple volt/hertz control of an induction motor was programmed. A smooth transition from linear to 12-step operation was showcased, accompanied by a significant reduction in the content of low-order harmonics. The impact was particularly pronounced in the case of the 5th and 7th harmonics, consistent with the results obtained from Fourier analysis.

References

[1] H. V. K. Salem, K. G. Robbersmyr, M. Norambuena, and J. Rodriguez, "Voltage source multilevel inverters with reduced device count: Topological review and novel comparative factors," *IEEE Trans. Power Electron.*, vol. 36, no. 3, pp. 2720–2747, Mar. 2021, doi: 10.1109/TPEL.2020.3011908.

[2] M. Trabelsi, H. Vahedi, and H. Abu-Rub, "Review on single-DC-source multilevel inverters: Topologies, challenges, industrial applications, and recommendations," *IEEE Open J. Ind. Electron. Soc.*, vol. 2, pp. 112–127, 2021, doi: 10.1109/OJIES.2021.3054666.

[3] M. Vijeh, M. Rezanejad, E. Samadaei, and K. Bertilsson, "A general review of multilevel inverters based on main submodules: Structural point of view," *IEEE Trans. Power Electron.*, vol. 34, no. 10, pp. 9479–9502, Oct. 2019, doi: 10.1109/TPEL.2018.2890649.

[4] A. Stillwell, E. Candan, and R. C. N. Pilawa-Podgurski, "Active voltage balancing in flying capacitor multi-level converters with valley current detection and constant effective duty cycle control," *IEEE Trans. Power Electron.*, vol. 34, no. 11, pp. 11429–11441, Nov. 2019, doi: 10.1109/TPEL.2019.289989.

[5] B. Jacob and M. R. Baiju, "A new space vector modulation scheme for multilevel inverters which directly vector quantize the reference space vector," *IEEE Trans. Ind. Electron.*, vol. 62, no. 1, pp. 88–95, Jan. 2015, doi: 10.1109/TIE.2014.2326998.

[6] A. K. Yadav, K. Gopakumar, R. R. K., L. Umanand, K. Matsuse, and H. Kubota, "Instantaneous balancing of neutral-point voltages for stacked DC-link capacitors of a multilevel inverter for dual-inverter-fed induction motor drives," *IEEE Trans. Power Electron.*, vol. 34, no. 3, pp. 2505–2514, Mar. 2019, doi: 10.1109/TPEL.2018.2837680.

[7] K. Wang, Z. Zheng, L. Xu, and Y. Li, "A generalized carrier-overlapped PWM method for neutral-point-clamped multilevel converters," *IEEE Trans. Power Electron.*, vol. 35, no. 9, pp. 9095–9106, Sep. 2020, doi: 10.1109/TPEL.2020.2969548.

[8] V. Jayakumar, B. Chokkalingam, and J. L. Munda, "A comprehensive review on space vector modulation techniques for neutral point clamped multi-level inverters," *IEEE Access*, vol. 9, pp. 112104–112144, 2021, doi: 10.1109/ACCESS.2021.3100346.

[9] H. Stemmler and P. Guggenbach, "Configurations of high-power voltage source inverter drives," in *Proc. 5th Eur. Conf. Power Electron. Appl.*, 1993, pp. 7–14, vol. 5.

[10] A. D. Kiadehi, K. E. K. Drissi, and C. Pasquier, "Voltage THD reduction for dual-inverter fed open-end load with isolated DC sources," *IEEE Trans. Ind. Electron.*, vol. 64, no. 3, pp. 2102–2111, Mar. 2017, doi: 10.1109/TIE.2016.2620420.

[11] S. Lakhimsetty, N. Surulivel, and V. T. Somasekhar, "Improvised SVPWM strategies for an enhanced performance for a four-level open-end winding induction motor drive," *IEEE Trans. Ind. Electron.*, vol. 64, no. 4, pp. 2750–2759, Apr. 2017, doi: 10.1109/TIE.2016.2632059.

[12] C. Sun, D. Sun, Z. Zheng, and H. Nian, "Simplified model predictive control for dual inverter-fed open-winding permanent magnet synchronous motor," *IEEE Trans. Energy Convers.*, vol. 33, no. 4, pp. 1846–1854, Dec. 2018, doi: 10.1109/TEC.2018.2841012.

[13] P. Naganathan and S. Srinivas, "Voltage-injected PWM variants for a dual two-level inverter-fed open-end winding induction motor drive," *IEEE J. Emerg. Sel. Topics Power Electron.*, vol. 9, no. 2, pp. 1532–1540, Apr. 2021, doi: 10.1109/JESTPE.2020.2972279.

[14] Z. Song, F. Zhou, Y. Yu, R. Zhang, and S. Hu, "Open-phase fault-tolerant predictive control strategy for Open-end-winding permanent magnet synchronous machines without postfault controller reconfiguration," *IEEE Trans. Ind. Electron.*, vol. 68, no. 5, pp. 3770–3781, May 2021, doi: 10.1109/TIE.2020.2984975.

[15] P. Sandulescu, F. Meinguet, X. Kestelyn, E. Semail, and A. Bruyère, "Control strategies for open-end winding drives operating in the flux-weakening region," *IEEE Trans. Power Electron.*, vol. 29, no. 9, pp. 4829–4842, Sep. 2014, doi: 10.1109/TPEL.2013.2283107.

[16] L. Rovere, A. Formentini, G. L. Calzo, P. Zanchetta, and T. Cox, "Zero-sequence voltage elimination for dual-fed common DC-link open-end winding PMSM high-speed starter–Generator—Part I: Modulation," *IEEE Trans. Ind. Appl.*, vol. 55, no. 6, pp. 7804–7812, Nov./Dec. 2019, doi: 10.1109/TIA.2019.2907073.

[17] Q. An, J. Liu, Z. Peng, L. Sun, and L. Sun, "Dual-space vector control of open-end winding permanent magnet synchronous motor drive fed by Dual inverter," *IEEE Trans. Power Electron.*, vol. 31, no. 12, pp. 8329–8342, Dec. 2016, doi: 10.1109/TPEL.2016.2520999.

[18] X. Lin, W. Huang, and L. Wang, "SVPWM strategy based on the Hysteresis controller of zero-sequence current for three-phase open-end winding PMSM," *IEEE Trans. Power Electron.*, vol. 34, no. 4, pp. 3474–3486, Apr. 2019, doi: 10.1109/TPEL.2018.2856372.

[19] S. Wdaan, C. Perera, and J. Salmon, "Maximum torque operation of open-winding induction motor dual drives using a floating capacitor bridge in the field weakening region," *IEEE Trans. Power Electron.*, vol. 37, no. 8, pp. 9629–9640, Aug. 2022, doi: 10.1109/TPEL.2022.3159483.

[20] Z. Huang, T. Yang, P. Giangrande, S. Chowdhury, M. Galea, and P. Wheeler, "Enhanced performance of dual inverter with a floating capacitor for motor drive applications," *IEEE Trans. Power Electron.*, vol. 36, no. 6, pp. 6903–6916, Jun. 2021, doi: 10.1109/TPEL.2020.3040029.

[21] H. Zhang, A. jouanne, and S. Dai, "A reduced-switch dual-bridge inverter topology for the mitigation of bearing currents, EMI, and DC-link voltage variations," *IEEE Trans. Ind. Appl.*, vol. 37, no. 5, pp. 1365–1372, Sep./Oct. 2001, doi: 10.1109/28.952512.

[22] K. B. Tawfiq, M. Güleç, and P. Sergeant, "Bearing current and shaft voltage in electrical machines: A comprehensive research review," *Machines*, vol. 11, no. 5, May 2023, Art. no. 550, doi: 10.3390/machines11050550.

[23] H.-W. Lee, S.-J. Jang, and K.-B. Lee, "Advanced DPWM method for switching loss reduction in isolated DC type dual inverter with open-end winding IPMSM," *IEEE Access*, vol. 11, pp. 2700–2710, 2023, doi: 10.1109/ACCESS.2023.3234296.

[24] T.-H. Kim, J.-H. Lee, B.-R. Yoon, and J.-S. Lee, "Clamping modulation technique for balancing power losses of dual inverter with isolated DC bus," *IEEE Access*, vol. 11, pp. 41868–41879, 2023, doi: 10.1109/ACCESS.2023.3270392.

[25] M. Chen and D. Sun, "A unified space vector pulse width modulation for dual two-level inverter system," *IEEE Trans. Power Electron.*, vol. 32, no. 2, pp. 889–893, Feb. 2017, doi: 10.1109/TPEL.2016.2585223.

[26] X. Guo, M. He, and Y. Yang, "Over modulation strategy of power converters: A review," *IEEE Access*, vol. 6, pp. 69528–69544, 2018.

[27] J. Zhou, S. Li, J. Zhang, T. Fang, and X. Zhang, "Research on space vector overmodulation technology of two-level PWM converters," *Energies*, vol. 15, no. 19, Sep. 2022, Art. no. 7086.

[28] S. Bolognani and M. Zigliotto, "Novel digital continuous control of SVM inverters in the overmodulation range," *IEEE Trans. Ind. Appl.*, vol. 33, no. 2, pp. 525–530, Mar./Apr. 1997.
[29] D. G. Holmes and T. A. Lipo, *Pulse Width Modulation for Power Converters: Principles and Practice*. Piscataway, NJ, USA: IEEE Press, 2003.
[30] M. L. De Klerk and A. K. Saha, "A comprehensive review of advanced traction motor control techniques suitable for electric vehicle applications," *IEEE Access*, vol. 9, pp. 125080–125108, 2021.

Filip Baum was born in Hořovice, the Czech Republic, in 1998. He recieved the M.S. degree in electrical drives, in 2023, from the Czech Technical University (CTU) in Prague, Prague, Czech Republic, where he is currently working toward the Ph.D. degree in electrical drives and power electronics at the Department of Electric Drives and Tranction, Faculty of Electrical Engineering.

Since 2020, he has been involved in research activities with the Department of Electric Drives and Tranction. His research interests include advanced modulation strategies of power converters and efficient controll of ac machines.

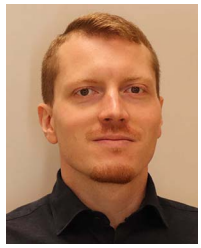

Ondrej Lipcak was born in Prague, the Czech Republic, in 1993. He received the M.Sc. and Ph.D. degrees in electrical machines, apparatus, and drives from the Faculty of Electrical Engineering, Czech Technical University (CTU) in Prague, Prague, Czech Republic, in 2018 and 2022, respectively.

Since 2018, he has been involved in research and teaching activities with the Department of Electric Drives and Traction, the CTU, where he became an Assistant Professor, in 2023. He is also currently involved in teaching several university courses on electrical machines, drives, and power electronics. His research interests include mathematical modeling, parameter estimation, and efficient control of ac machines and power electronics converters.